Population connective field modeling reveals proto-retinotopic visual cortex organization in the prenatal human brain

So-Hyeon Yoo[1], Anne-Sophie Kieslinger[1] and Michael A. Skeide[1] ✉

[1] Research Group Learning in Early Childhood,
Max Planck Institute for Human Cognitive and Brain Sciences,
Stephanstraße 1A, 04103 Leipzig, Germany

✉e-mail: skeide@cbs.mpg.de

Correspondence should be addressed to Michael A. Skeide

Abstract

The visual space is sampled by cortical field maps in which nearby neuronal populations encode nearby locations of images received from the retina. Whether retinotopic cortical organization already emerges in the neonatal or even prenatal human brain is currently unknown. To answer this question in vivo, we applied population connective field modeling to 471 resting-state functional magnetic resonance imaging datasets ranging from prenatal to young adult age. We found topographically organized eccentricity and polar angle connectivity maps in V2 and V3 of the visual cortex as early as the 21st week of gestation. These results highlight that human proto-retinotopic cortical maps develop in the second trimester of pregnancy, predating visual experience.

Introduction

Visual cortices transform input signals from the retina into internal representations of the visual space providing the foundation for perceiving and interpreting environments[1]. These cortices are organized retinotopically, such that nearby locations of the retinal image are encoded by nearby neuronal populations[2,3]. In retinotopic maps, nearby neuronal populations encode eccentricity, that is, the distance from the center of the visual space. Specifically, the cortical surface area representing visual space decreases with increasing eccentricity towards anteromedial visual cortices[4–7]. Nearby neuronal populations also encode polar angle, that is, the angular distance between a location in visual space relative to an axis, like the vertical meridian. Polar angle progression in the opposite direction at the boundary between subregions of the visual cortex is considered a critical feature of retinotopic organization[5–7].

While retinotopic visual cortex organization has been extensively studied in the adult brain, its emergence in the developing brain remains poorly understood[1]. Functional magnetic resonance imaging (fMRI) studies show that eccentricity and polar angle maps are in part qualitatively similar to adults by the age of 5 years except that children have a similar amount of V1 surface area representing the lower and upper vertical meridians of the visual space[8-10]. In macaque monkeys, however, retinotopically organized eccentricity and polar angle maps have been identified already at the neonatal stage using fMRI[11]. Other proto-retinotopic features, including response preferences for horizontal and vertical orientation as well as high and low spatial frequencies have been revealed by fMRI in infants aged 5 months[12]. Whether proto-retinotopic organization is present in neonatal, let alone prenatal humans, is currently unknown.

To answer this question, we applied population connective field modeling to 471 resting-state fMRI datasets from the Human Connectome Project including prenatal, neonatal, adolescent, and adult

age groups[13,14]. Population connective field modeling serves to estimate the dependence between hemodynamic signals in distinct cortical regions by predicting responses in a region as a function of activity in another region based on a Gaussian function[15]. This method has been validated against the widely used population receptive field modeling approach using task-based fMRI signals evoked by visual stimuli[15]. In addition, this method has also been validated against task-free resting-state fMRI signals in V1, V2 and V3[16]. Accordingly, population connective field modeling of resting-state fMRI data allowed us to examine proto-retinotopic organization in prenatal subjects who are not able to engage in a visual field mapping task. Here, we used a retinotopy template that was derived from task-based fMRI data collected in adults during visual receptive field mapping experiments. Warping this template into native space we identified the regions of interest V1, V2 and V3, then employed population connective field modeling to find resting-state hemodynamic time series in V1 that correlated most strongly with corresponding time series in V2 and V3, and finally inferred eccentricity and polar angle values in V2 and V3 from the values in V1 given by the template[15–17]. Differences in data quality across datasets were adjusted with an empirical Bayesian framework for group comparison analyses. This framework also accounted for possible site effects on data acquisition, for example, related to hardware and software factors in different scanning environments.

Given that retinotopic maps have been identified in newborn macaques[11], we hypothesized that topographically organized eccentricity and polar angle maps in humans can be identified only from a neonatal age onwards. Contrary to our hypothesis, however, we found topographically organized eccentricity and polar angle connectivity maps already from prenatal age onwards, as early as in the 21st week of gestation.

Results

Group characteristics

Prenatal MRI scans recorded during the second trimester of pregnancy (here between 21 and 28 weeks gestational age) and the third trimester of pregnancy (≥29 weeks gestational age) were compared against preterm neonatal data (born <37 weeks gestational age) and full-term neonatal data (born ≥37 weeks gestational age) as well as MRI scans recorded during adolescence (12–16 years) and early adulthood (18–21 years). All six groups included cross-sectional data of different subjects (Table 1). Preterm neonatal data were not excluded since we aspired to examine whether proto-retinotopic maps would develop typically in this population which is known to be at risk for neurodevelopmental disorders[18,19].

Table 1 | Group characteristics.

	tri-2[2] prenatal	**tri-3[3] prenatal**	**preterm neonatal**	**full-term neonatal**	**adolescent**	**adult**
mean scan age	26.10[4]	32.00[4]	38.04[4]	41.44[4]	14.11[5]	20.21[5]
scan age range	21–28[4]	29–36[4]	34–44[4]	37–44[4]	12–16[5]	18–21[5]
sex (f/m)[1]	55/54	41/55	20/21	48/63	37/23	32/22
n subjects	109	96	41	111	60	54

[1]female/male [2/3]second/third trimester of pregnancy [4]age in weeks [5]age in years

Controlling for anatomical differences, data quality and site effects

To account for possible anatomical effects of brain size and cortical morphology, such as gyrification and sulcal patterns, on registration quality, a step-wise transformation procedure was applied to register structural images to an adult surface template containing both the dorsal and ventral visual regions of interest V1, V2 and V3 (see Methods, subsection on retinotopic template projection, for

details). Individual examples demonstrating image registration results across different age groups are provided in Supplementary Fig. S1.

Temporal signal-to-noise ratio (tSNR) in V1–V3 differed significantly between the six groups ($\chi^2(5) = 364.63$, $\eta^2 = 0.88$, bootstrapped $p < 0.001$, Kruskal-Wallis test) (see Supplementary Fig. S2 for pairwise group comparisons). Accordingly, to account for these differences in data quality and also for data acquisition site effects in direct statistical group comparisons, eccentricity and polar angle values obtained from the population connective field model were adjusted for tSNR values and sites by using a parametric empirical Bayesian framework[20].

Population connective field modeling

Hemodynamic time courses estimated by the population connective field model in V1 of the visual cortex were first correlated with observed hemodynamic time courses measured in V2 and V3. Eccentricity and polar angle values were then obtained from a template that was derived from event-related fMRI data collected in adults during visual receptive field mapping experiments (Fig. 1 and 2). To this end, template values at each vertex in V1 were projected to the vertex in V2 and V3 that was fit best by the model as indicated by the highest positive correlation coefficient. Finally, we confirmed statistically that associations between the connective field model and the retinotopic template data did not arise by chance. Accordingly, eccentricity and polar angle values obtained from the empirical hemodynamic signal were compared with values obtained from simulated random hemodynamic signals (Supplementary Fig. S5 and S8).

Eccentricity connectivity mapping

Mapping eccentricity values onto the surfaces revealed topographic increases with distance from the occipital pole towards anteromedial V2 and V3 in all groups (Fig. 1). Moreover, probability density histograms demonstrated that, in all groups, by far most vertices most likely represent small eccentricities close to the center of the visual space (Fig. 1). At the same time, we found significant group differences between eccentricity maps and the number of significant vertices gradually increased with increasing age differences (see Supplementary Fig. S3). Examples of individual eccentricity maps across the different age groups are provided in Supplementary Fig. S4. In all groups and in both hemispheres, the connective field model applied to the empirical data fit the eccentricity template better than simulated data, as indicated by comparing mean squared differences (all $z \geq 5.58$, all $p < 0.001$, Wilcoxon signed-rank tests; see Supplementary Fig. S5 for distributions of mean squared differences across all groups).

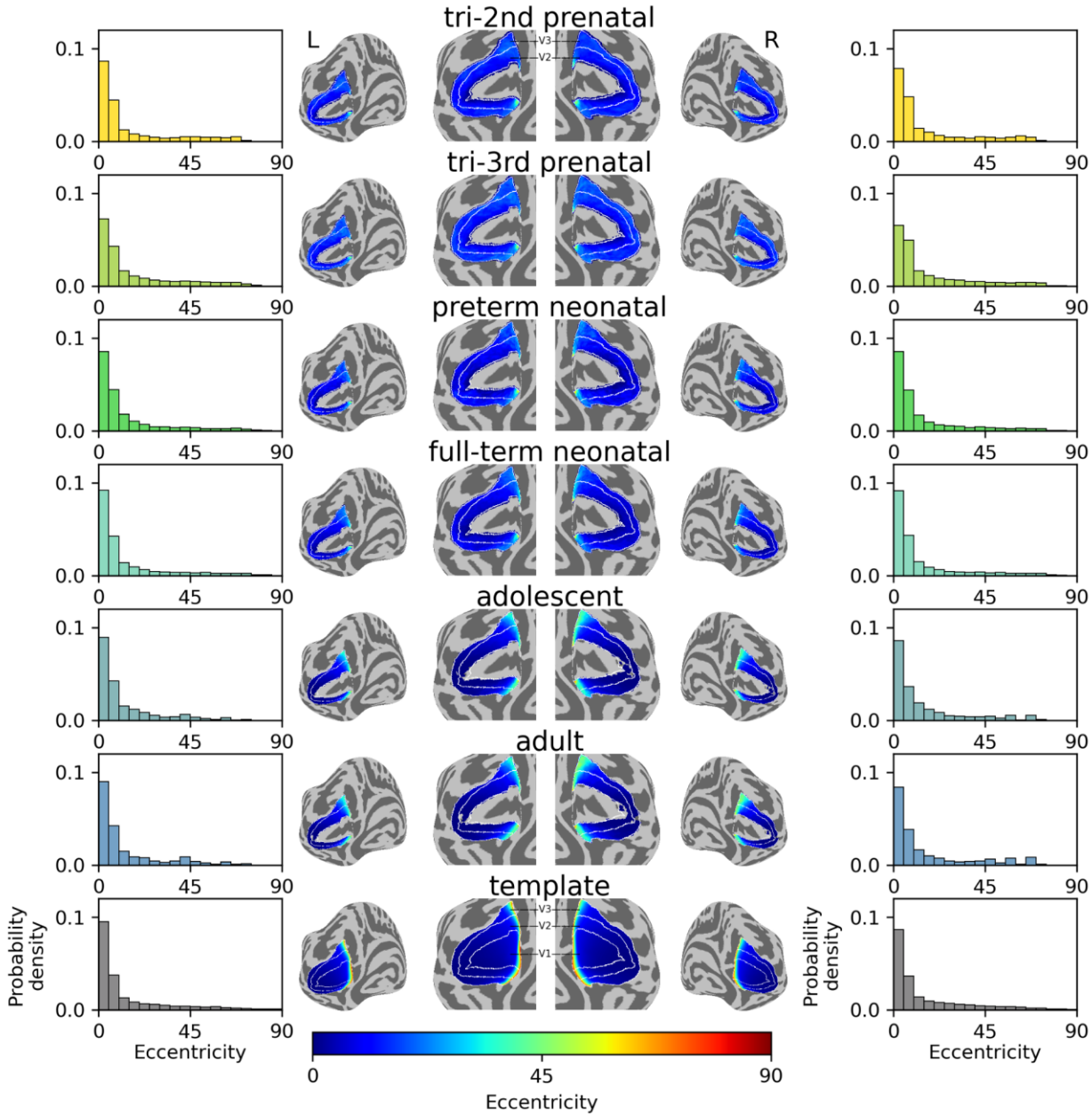

Fig. 1 | Eccentricity maps. Eccentricity values were obtained from a template (shown in the bottom row) generated using event-related fMRI data collected in a receptive field mapping experiment. Maps were averaged within each group. L = left hemisphere, R = right hemisphere. White lines demarcate V1, V2, and V3. The color bar indicates eccentricity (degrees from the fovea). Histograms summarize probability densities across all subjects and regions of interest (V2 and V3) separately for each hemisphere.

Polar angle connectivity mapping

At the boundaries between V1, V2 and V3, the progression of polar angle reversed direction in all groups (Fig. 2). To quantitatively confirm polar angle reversal we also computed gradients representing the direction of change within vertex-wise polar angle values. Mean gradients in a dorsal-to-ventral coordinate system indicated that polar angle in V2 and V3 indeed progressed in opposite directions in all groups (Fig. 3). There were also significant group differences between polar angle maps and the number of significant vertices gradually increased with increasing age differences (see Supplementary Fig. S6). Examples of individual polar angle maps across the different age groups can be found in Supplementary Fig. S7. In all groups and both hemispheres, the connective field model applied to the empirical data fit the polar angle template better than the simulated data (all $z \geq 5.58$, all $p < 0.001$, Wilcoxon signed-rank tests; see Supplementary Fig. S8 for distributions of mean squared differences across all groups).

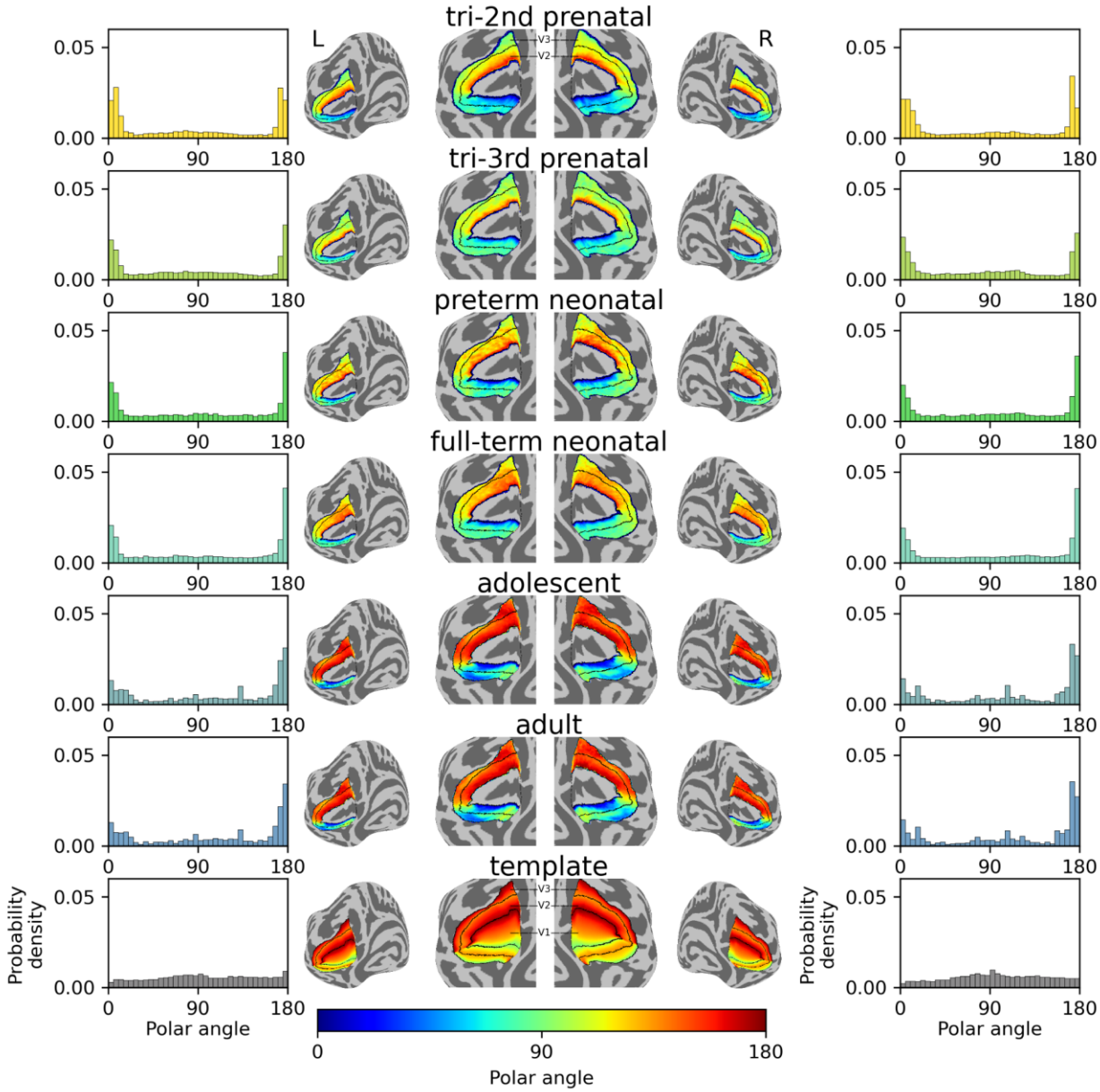

Fig. 2 | Polar angle maps. Polar angle values were obtained from a template (shown in the bottom row) generated using event-related fMRI data collected in a receptive field mapping experiment. Maps were averaged within each group. L = left hemisphere, R = right hemisphere. Black lines demarcate V1, V2, and V3. The color bar indicates polar angle (angular distance from the vertical meridian in degrees). Histograms summarize probability densities across all subjects and regions of interest (V2 and V3) separately for each hemisphere (left and right).

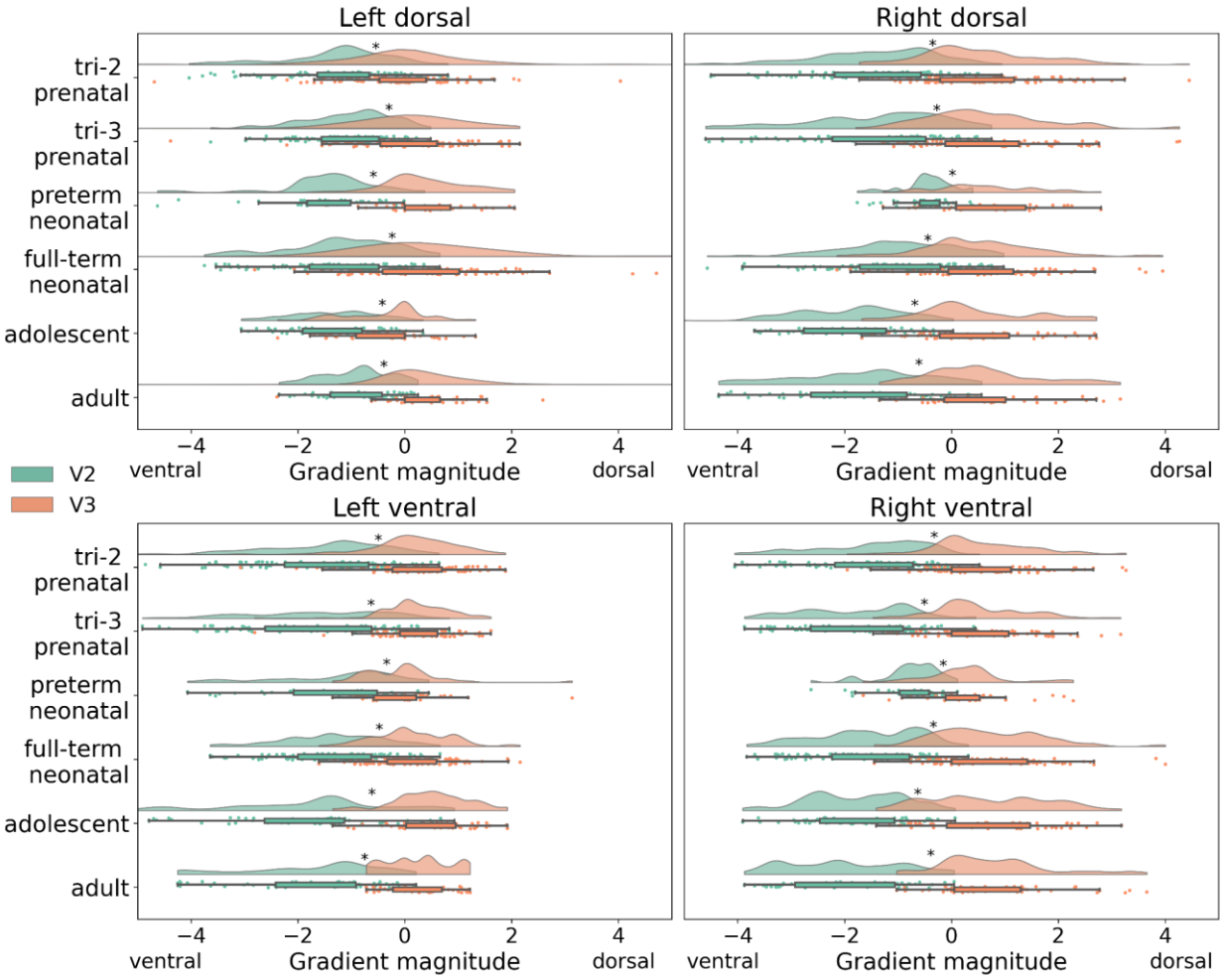

Fig. 3 | Mean gradient directions of polar angle values. Mean gradient magnitudes were computed to quantify dorsal and ventral directions of polar angle progression. To this end, V2 (green) and V3 (orange) were partitioned into dorsal and ventral subregions. x-axes depict the magnitude of the gradients and y-axes depict the different age groups. Negative values indicate ventral progression while positive values indicate dorsal progression. Curves illustrate probability density while lines illustrate the lengths of the distributions. Box plots visualize upper and lower quartiles. Asterisks indicate statistically significant differences at a bootstrapped threshold of $p < 0.001$ (Wilcoxon signed-rank tests).

Discussion

Population connective field modeling of developmental resting-state fMRI data revealed a proto-retinotopic organization of visual cortices in prenatal human brains. Already in the 21st gestational week, eccentricity increased towards anteromedial V2 and V3 of the visual cortex and polar angle progressed in opposite directions in V2 and V3.

Human visual population receptive fields are traditionally mapped using task-based fMRI. This technique, however, is not applicable to prenatal subjects and has not yet been successfully applied to neonatal subjects. Accordingly, population connective field modeling was employed in this study to reconstruct retinotopic features from resting-state fMRI data in the absence of a visual task. The task-free resting-state fMRI results reported here can be explained by animal models based on the observation that temporally coupled stimulus-independent neural activity is necessary for the development of visual receptive field properties related to retinotopic maps[21–24]. Such spontaneous activity is thought to strengthen or maintain correctly targeted synaptic connections. Synchronized stimulus-independent firing can be observed in primate and rodent visual cortex well before behavioral signs of visual processing emerge and even before photoreceptors respond to light[21–24]. Future studies using longitudinal high-field MRI in humans might be able to shed light on these processes in vivo and noninvasively at a mesoscopic scale capturing layer-specific hemodynamic responses and fiber projections.

Proto-retinotopic organization of eccentricity and polar angle maps in the second trimester of pregnancy is remarkable from a behavioral perspective since the eyes typically open only by 28 weeks of gestation, pupils constrict and dilate only at around 31 weeks of gestation, and the fetus orients to external laser light stimuli only by around 34 weeks of gestation[25,26]. Furthermore, from an environmental perspective, biophysical modeling results suggest that intrauterine illumination is severely limited by maternal tissue[27]. There is fMRI evidence, however, that resting-state retinotopic organization emerges without visual experience even in congenitally blind adults[16]. Furthermore, these results in humans are supported by single-cell recording and photon imaging studies in rodents. These

184 studies show that, already at eye opening, the proportion of receptive fields and the angle of visual
185 space they represent is similar to more mature animals[28]. At the same time, despite these similarities,
186 neural responses become more reliable in the course of further brain development[28]. Such maturation
187 effects could be related to the present finding that age group differences between eccentricity and polar
188 angle maps gradually increased with increasing age differences.

189 The connective field mapping approach taken here requires a flattened cortical surface
190 template that allows to predict the location and topographic organization of visual areas from cortical
191 anatomy alone. Such templates are currently only available for eccentricity and polar angle[17]. Future
192 work should consider applying population connective field modeling to additional retinotopic features
193 including orientation tuning and spatial frequency tuning if they become available[12]. Another aspect to
194 be addressed is that the retinotopic feature templates used for the present study are derived from task-
195 based fMRI in adults. It is an open question whether such templates could also be derived from neonatal
196 infants despite the considerable challenges inherent to task-based fMRI in this population.

197 To account for differences in data quality and site effects data were adjusted with an empirical
198 Bayesian framework for direct statistical comparison across prenatal, neonatal, adolescent and adult
199 groups. In the other analyses, we desisted from adjustment to avoid introducing biases into the
200 population connective field model estimation. This decision is based on previous work demonstrating
201 that connective field size estimates are robust to differences in signal-to-noise ratio[16]. Contributions of
202 other factors beyond our analytical control, such as more variable signals in the younger developmental
203 groups, remain to be ruled out in future investigations[29,30].

204

205 **Methods**

206 **Participants**

207 **Prenatal and neonatal participants.** Prenatal and neonatal participants were recruited between 2015
208 and 2019 at St Thomas' Hospital in London for the Developing Human Connectome Project. Written
209 informed consent of all legal guardians was obtained for all participants prior to taking part in the study.

210 All study procedures were reviewed and approved by the London-Riverside Research Ethics Committee
211 of the Health Research Agency (REC: 14/Lo/1169)[14,31]. The analysis of the pre-existing data was approved
212 by the Ethics Committee at the Medical Faculty of the University of Leipzig, Germany (IRB00001750).
213 109 unique prenatal datasets corresponding to the second trimester of pregnancy (between 21
214 and 28 weeks gestational age) and 96 unique prenatal datasets corresponding to the third trimester of
215 pregnancy (≥29 weeks gestational age) were included in the current study (mean gestational age 32.00
216 weeks, range 29–36 weeks). Additionally, we included 41 preterm neonates born <37 weeks gestational
217 age (mean gestational age 32.46 weeks, range 23–36 weeks). 27 neonates admitted to neonatal
218 intensive care, nine neonates with incomplete or abandoned scans, one neonate with vermian
219 hypoplasia and one neonate with congenital heart disease were excluded from the study. The final
220 cohort of 111 full-term neonates born ≥37 weeks gestational age (mean gestational age 39.98 weeks,
221 range 37–42 weeks) had normal findings on clinical examination by a neonatologist prior to MRI data
222 acquisition. Neuroradiological inspection of the MRI data mostly revealed clinically insignificant
223 incidental findings[32]. Regardless of a potential clinical significance, incidental findings with unlikely
224 measurable relevance for functional connectivity analysis were permissible[32]. However, in line with the
225 guidelines of the Developing Human Connectome Project, we excluded datasets with incidental
226 findings that might have a possible impact on the analyses in accordance with radiological ratings.
227 **Adolescent and adult participants.** Adolescent and adult participants were recruited between
228 2017 and 2019 in Boston, Los Angeles, Minneapolis and St. Louis for the Human Connectome Project –
229 Development. Written informed consent of all legal guardians was obtained for all participants prior to
230 taking part in the study. All study procedures were reviewed and approved by a central institutional
231 review board at Washington University in St. Louis. The analysis of the pre-existing data was approved
232 by the Ethics Committee at the Medical Faculty of the University of Leipzig, Germany (IRB00001750).
233 60 unique adolescent datasets (mean scan age 14.49 years, range 12–17 years) and 54 unique
234 early adult datasets (mean scan age 20.21 years, range 18–21 years) were included in the current study.
235 289 datasets that did not pass the quality control procedure were excluded from our analysis (see Data

236 Preprocessing below). We also excluded 34 subjects with visual impairments. Neuroradiological
237 inspection of the MRI data revealed no clinically significant incidental findings
238
239 **Data acquisition**
240 **Prenatal and neonatal data.** Prenatal and neonatal images were collected on a 3T Philips Achieva
241 scanner with a neonatal 32-channel phased-array head coil at the Evelina London Children's Hospital.
242 These data are publicly available as part of the fourth release of the Developing Human Connectome
243 Project (https://biomedia.github.io/dHCP-release-notes/) and were accessed in the National Institute
244 of Mental Health Data Archive (NDA)[14].
245 Data were acquired without sedation. Neonates were scanned during natural sleep following
246 feeding and swaddling in a vacuum-evacuated blanket. To standardize pose, subjects were placed in a
247 cradle. Hearing protection was provided in the form of molded dental putty, Minimuffs on-ear noise
248 attenuators, and an acoustic hood[33].
249 For structural imaging, a T2-weighted fast spin echo image was acquired twice with TR = 12 s,
250 TE = 156 ms, SENSE factor: axial = 2.11 and sagittal = 2.58, 290 × 290 × 203 voxels, voxel size 0.8 mm x 0.8
251 mm x 1.6 mm (overlapped by 0.8 mm). In addition, a T1-weighted inversion recovery fast spin echo
252 image was acquired twice with TR = 4,795 ms, TE = 8.7 ms, SENSE factor: axial = 2.26 and sagittal = 2.66
253 and matched to the T2-weighted image in terms of number of voxels and voxel size[34].
254 For functional imaging, 2,300 T2*-weighted single-shot echo-planar imaging volumes were
255 acquired with TR = 392 ms, TE = 38 ms, flip angle = 34°, multiband acceleration factor of 9, 67 × 67 × 45
256 voxels, voxel size 2.15 mm x 2.15 mm x 2.15 mm. Single-band reference scans were also acquired with
257 bandwidth-matched readout, along with additional spin-echo echo-planar imaging acquisitions
258 (fieldmaps) with 4 x AP and 4 x PA phase-encoding directions[34].
259 **Adolescent and adult data.** Adolescent and adult data were collected on 3T Siemens Prisma
260 scanners with 32-channel head coils at Harvard University, University of California at Los Angeles,
261 University of Minnesota, and Washington University in St. Louis. These data are publicly available as

262 part of the second release of the Human Connectome Project – Development and were accessed in the
263 National Institute of Mental Health Data Archive (NDA)[13].
264 For structural imaging, a T2-weighted variable-flip-angle turbo-spin-echo image was acquired
265 with TR = 3,200 ms, TE = 564 ms, 320 × 300 × 208 voxels, voxel size 0.8 mm x 0.8 mm x 0.8 mm). In addition,
266 a T1-weighted multi-echo image was acquired twice with TR = 2,500 ms, TE1 = 1.81 ms, TE2 = 3.6 ms,
267 TE3 = 5.39 ms, TE 4 = 7.18 ms and matched to the T2-weighted image in terms of number of voxels and
268 voxel size. Subjects watched a movie during these procedures[35].
269 For resting-state functional imaging, 488 T2*-weighted single-shot echo-planar imaging
270 volumes were acquired four to six times with TR = 800 ms, TE = 37 ms, flip angle = 52°, multiband
271 acceleration factor of 8, 67 × 67 × 45 voxels, voxel size 2 mm x 2 mm x 2 mm. Subjects were instructed to
272 look at a fixation cross during this procedure. A single-band spin-echo echo-planar imaging fieldmap
273 with one AP and one PA phase-encoding direction was also acquired with bandwidth-matched
274 readout[35].
275
276 **Data preprocessing**
277 **Developing Human Connectome Project: Prenatal and neonatal images**
278 **Structural image preprocessing.** T2-weighted structural images were pre-processed according to the
279 structural pipeline developed in the developing human connectome project (dHCP)[36]. First, motion
280 correction and super-resolution reconstruction techniques were employed on T1- and T2-weighted
281 structural images[37,38]. Second, the reconstructed T1- and T2-weighted images were bias-corrected using
282 the N4 bias field correction algorithm[39] and the Brain Extraction Tool (BET) implemented in the FSL
283 software package (5.0.11)[40]. Finally, each T1-weighted image was registered rigidly to the
284 corresponding T2-weighted image using the Medical Image Registration ToolKit (MIRTK).
285 After preprocessing, the T2-weighted images were segmented into different tissue types (white
286 matter, cortical gray matter, subcortical gray matter, and cerebrospinal fluid) using the Developing
287 brain region annotation with Expectation-Maximization (Draw-EM) algorithm[41]. Draw-EM was also

288 employed to generate surface meshes (white matter, pial, and mid-thickness surfaces). Only those
289 datasets that exhibited an identical number of vertices in the white matter and pial meshes following
290 the reconstruction of surface data were subjected to further analysis. This step is necessary as the
291 vertices in white matter and pial mesh form a triangular prism when resampling a volume image to a
292 surface image. During this process, the signals of multiple voxels in the triangular prism are restructured
293 into a single time series. Accordingly, if the number of vertices in white matter and pial meshes are
294 different, volume-to-surface mapping fails. 95 out of 136 preterm datasets and 346 out of 457 full-term
295 datasets with this quality issue were excluded from further analysis.

296 **Functional image preprocessing.** T2*-weighted functional images were preprocessed in
297 accordance with the resting-state functional processing pipeline in the dHCP[34]. First, local signal
298 distortions resulting from magnetic field inhomogeneities were corrected using the FSL TOPUP tool[42].
299 Second, slice-to-volume and rigid-body realignment were employed using the FSL EDDY tool[43] to
300 correct for in- and out-of-volume head motion and dynamic distortions. Third, a high-pass filter with a
301 150s cutoff was applied to remove slow drifts. Finally, residual head motion, motion artifacts arising
302 from multiband acceleration, and physiological noise were removed using a linear regression model
303 implemented in FMRIB's ICA-based Xnoiseifier tool (FIX, v1.066)[44].

304

305 **Human Connectome Project: Adolescent and adult images**

306 **Structural image preprocessing.** T1- and T2-weighted structural images were preprocessed according
307 to the structural pipeline of the Human Connectome Project (HCP-D). This pipeline comprises three
308 preprocessing stages: PreFreeSurfer, FreeSurfer and PostFreeSurfer. In PreFreeSurfer, structural
309 images were distortion-corrected, aligned, and registered to the Montreal Neurological Institute (MNI)
310 standard space using the FMRIB software library implemented in FSL. In FreeSurfer, structural cortical
311 maps are reconstructed by employing the recon-all pipeline. In PostFreeSurfer, a brain mask, a cortical
312 ribbon volume image, and cortical myelin maps are generated. Finally, the surface mesh in native space
313 is resampled into fs-LR space[45].

Functional image preprocessing. T2*-weighted functional images were preprocessed in accordance with the resting-state functional processing pipeline of the HCP-D[35,45]. First, volumes were preprocessed using FSL FLIRT to correct for head motion and dynamic distortions[46]. FSL FLIRT was also employed for non-linear alignment to the MNI standard space. Second, distortions in the phase encoding direction were estimated using FSL TOPUP[42]. Third, volumes were resampled from standard space to a surface representation consisting of 91,282 gray matter coordinates. Fourth, gray matter ribbons were determined in native space with the fslmaths tool in FSL and mapped to the gray matter coordinates surface using the Connectome Workbench tool (v1.4.2). Fifth, head motion indices and independent components were regressed out using FMRIB's ICA-FIX (v.1.0.6.14). In the final step, images were re-registered to the cortical surfaces using MSMAll (v.1.0)[47].

Population connective field modeling analysis

Registration of functional images from volume to surface space. Structural surfaces in native T2-weighted image space were warped into the native volume space of the functional images using the affine transformation matrices generated by dHCP (boundary-based registration, FSL FLIRT). Subsequently, functional volumetric data were projected to the resulting surface using the ribbon-constrained mapping approach implemented in the Connectome Workbench tool (v1.5.0). Regions of interest were primary, secondary, and third visual cortices (V1, V2 and V3) defined by Benson's anatomical template[17].

Population connective field model estimation. Population connective field modeling has been described comprehensively by Haak and colleagues (2013)[15]. First, hemodynamic time series for each vertex in V1, V2, and V3 were converted to time series of percent signal change.

$$a_v(t) = \{s_v(t) - mean_v\} \times 100,$$

where, $a_v(t)$ and $s_v(t)$ represent the percent signal change and the raw signal of the vertex v at time point t, respectively, and $mean_v$ is a time-averaged raw signal of the vertex v.

Next, candidate connective fields were specified. The cortical connective field for each vertex v in the target region $V2$ and $V3$ consists of weights for each vertex w in the source region $V1$, with w_0 denoting the center vertex of the connective field in the source region $V1$. Each candidate connective field model is a Gaussian distribution defined by its center vertex w_0 and its spread σ over the cortical surface.

$$g_{w_0,\sigma}(w) = exp(-\frac{d(w_0,w)^2}{2\sigma^2}),$$

where, $d(w_0, w)$ indicates the shortest distance from the center vertex w_0 to all other vertices w in the source region along the cortical surface mesh and $g_{w_0,\sigma}(w)$ indicates the connective field weights for all w, centered on w_0 with spread σ. Distances between vertices were calculated along the pial surface using a Scipy (v1.12.0) implementation of the Dijkstra algorithm in Python (v3.11.7).

For each connective field g, the weights of the cortical field in the surface mesh were then used to compute a time series. The time series $a_w(t)$ of all vertices w in $V1$ are weighted by their contribution to the cortical field $g_{w_0,\sigma}(w)$ and summed up to constitute the time series of the connective field $c_{w_0,\sigma}(t)$.

$$c_{w_0,\sigma}(t) = \sum_{w} a_w(t) \cdot g_{w_0,\sigma}(w)$$

The fit of the connective field model was defined as the Pearson correlation between the time series of the connective field and the time series of the vertex in V2 and V3. For an initial parameter search, candidate time series of the connective field were calculated for all V1 vertices and 10 cortical spread values σ between 3 and 25 mm. A non-linear optimization over spread σ was performed for all vertices, using the Broyden-Fletcher-Goldfarb-Shanno algorithm implemented in Scipy's optimization module.

Null model estimation on simulated data. To create a null model without retinotopically organized signals, hemodynamic surface data in V1, V2 and V3 were simulated using a local correlation model. For each surface vertex, a random time series was generated from a normal distribution with the same number of timepoints as the empirically measured hemodynamic data. The local correlations in V1, V2 and V3 were then smoothed using a Gaussian filter with a kernel width of 30 mm and adjusted to match the median local correlation coefficient of the empirical data using Cholesky decomposition.

364 **Retinotopic template projection.** Retinotopic maps containing eccentricity and polar angle
365 values were derived from an adult template[17]. As the template was defined on the fsaverage surface
366 mesh template in FreeSurfer, it was necessary to warp the template from fsaverage space to native
367 space. Due to the structural differences between developing and adult brains, a direct transformation
368 from fsaverage to native space could introduce misalignment or distortions. Accordingly, a four-step
369 registration procedure was applied to the retinotopy templates instead, including (1) registration from
370 fsaverage space to the space of the young adult template of the Human Connectome Project (HCP), (2)
371 registration from young adult space to the space of the 40-week template of the dHCP[44] (see
372 https://t.ly/AFwNT for both hemispheres), (3) registration from 40-week space to the space of an age-
373 matched group template, and (4) registration from the age-matched group template space to native
374 space.

375 For the first registration step, we used the registration sphere of the HCP young adult mesh
376 deformed to fsaverage, available from the HCP[44]. For the second registration step, we used an existing
377 sphere generated during the transformation of the dHCP 40-week template sphere to the HCP sphere[31].
378 For the third registration, we used an existing sphere that was generated in the dHCP by transforming
379 an age-matched template sphere to the 40-week template sphere. For the fourth registration, the native
380 surface sphere was rotated to align with HCP fsLR volumetric space and then registered to the age-
381 matched template sphere of the dHCP using the Biomedical Imaging Analysis Group's Medical Image
382 Restoration Toolkit (MIRTK) and the newMSM software package (v.0.5.1-BETA), following the procedure
383 implemented in https://github.com/ecr05/dHCP_template_alignment. As a final step, these four
384 registrations were concatenated and used to resample the template from fsaverage space to native
385 space. The transformation and concatenation of all registrations was performed using the Human
386 Connectome Project workbench toolkit (v1.5.0). As the preprocessed resting-state fMRI data provided
387 by the HCP is resampled in fs-LR space, registration was performed only once from fs-LR to fsaverage
388 space. All remaining analysis steps were identical between the HCP and dHCP data.

In each subject, connective field modeling was conducted in native space using a warped template. Subsequently, maps were warped into fsaverage space for further statistical analysis of unthresholded correlation coefficients as well as connective field size, eccentricity, and polar angle values. Vertex-wise eccentricity and polar angle values were assigned to the most strongly positively correlated seed vertex.

Local gradient analysis. To quantitatively assess the direction of change in the V2 and V3 polar angle values, we computed a gradient at each vertex in a right-to-left, anterior-to-posterior and dorsal-to-ventral coordinate system. A gradient was defined as the sum of the difference between polar angle values of neighboring vertices multiplied by the differences between one vertex and neighboring vertices (vectors) divided by the sum of the squared Euclidean norm of the differences between vectors. If the number of connected vertices of a vertex is *n*, the gradient at vertex *k* is calculated as follows:

$$gradient_k \approx \frac{\sum_{i=1}^{n} (p_i - p_k)(v_i - v_k)}{\sum_{i=1}^{n} \left|\left|v_i - v_k\right|\right|^2}$$

where *p* is the polar angle value of the vertex and *v* is a position vector of the vertex in a three-dimensional real coordinate space $\Re^3$. V2 and V3 were subdivided into dorsal and ventral regions in accordance with the template created by Wang and colleagues[48] to allow for a more detailed group comparison.

Statistical analyses

Adjustment for data quality and site effects. A parametric empirical Bayesian framework implemented in the *neuroCombat* Python library was employed to rectify connectivity results for differences in data quality and site effects[49]. This framework incorporates age and sex as variables to be retained, while adjusting estimates for effects of no interest, including site, the averaged tSNR of V1 and the tSNR of each vertex in V2-3.

Group comparison of connective field distributions. To ascertain whether the connective field estimates within each region of interest exhibit differential distributions across age groups, we

employed bootstrapped Kruskal-Wallis tests written in custom Python code. The Kruskal-Wallis test allowed us to determine whether at least one group stochastically dominated at least one other group. Effect size was calculated as the square root of dividing the Kruskal-Wallis test statistic by the number of observations. The χ^2 value was calculated by randomly resampling the subjects 10,000 times in all groups, using the same number of subjects in the original group and allowing duplication using SciPy's *kruskal* function. Effect sizes of Kruskal-Wallis tests were calculated based on the following formula:

$$effect\ size\ (\eta^2) = \frac{H\ statistic\ -\ number\ of\ groups\ +\ 1}{number\ of\ total\ observation\ -\ number\ of\ groups}$$

In the case of significant evidence for stochastic dominance, Mann-Whitney-U tests were performed vertex-wise for each pair of age groups. Mann-Whitney-U tests were carried out to compare pairs of groups using Scipy's *mannwhitneyu* function. For paired group comparison, a bootstrap mean difference test was conducted by randomly resampling 10,000 times.

Comparison of connective field modeling results for measured and simulated data. We compared the results of the connective field model applied to the measured fMRI data in the V2 region (1) with the retinotopic values (eccentricity and polar angle) of Benson et al.'s template and (2) with the results of the connective field model applied to simulated fMRI data. For model comparison, we calculated the mean squared difference (MSD).

The following formula was employed to calculate the MSD values:

Measured data vs. Benson template: $MSD_{Benson} = \frac{1}{n}\sum_{i=1}^{n} \quad (p - p_{Benson})^2$,

Measured data vs. Simulated data: $MSD_{Simulated} = \frac{1}{n}\sum_{i=1}^{n} \quad (p - p_{Simulated})^2$.

where n is the number of vertices and p is the connective field parameter value of interest for each vertex. Statistical differences between MSD values were calculated based on Wilcoxon signed-rank tests. Wilcoxon signed-rank tests were performed using Scipy's *wilcoxon* function.

References

1. Himmelberg, M. M., Winawer, J. & Carrasco, M. Polar angle asymmetries in visual perception and neural architecture. *Trends Neurosci.* **46**, 445–458 (2023).
2. Hubel, D. H. & Wiesel, T. N. Uniformity of monkey striate cortex: A parallel relationship between field size, scatter, and magnification factor. *J. Comp. Neurol.* **158**, 295–305 (1974).
3. Tootell, R. B. H., Silverman, M. S., Switkes, E. & De Valois, R. L. Deoxyglucose analysis of retinotopic organization in primate striate cortex. *Science* **218**, 902–904 (1982).
4. Engel, S. A. *et al.* fMRI of human visual cortex. *Nature* **369**, 525–525 (1994).
5. Sereno, M. I. *et al.* Borders of multiple visual areas in humans revealed by functional magnetic resonance imaging. *Science* **268**, 889–893 (1995).
6. Benson, N. C. *et al.* The Human Connectome Project 7 Tesla retinotopy dataset: Description and population receptive field analysis. *J. Vis.* **18**, 23–23 (2018).
7. Himmelberg, M. M. *et al.* Cross-dataset reproducibility of human retinotopic maps. *Neuroimage* **244**, 118609 (2021).
8. Gomez, J., Natu, V., Jeska, B., Barnett, M. & Grill-Spector, K. Development differentially sculpts receptive fields across early and high-level human visual cortex. *Nat. Commun.* **9**, 1–12 (2018).
9. Dekker, T. M., Schwarzkopf, D. S., de Haas, B., Nardini, M. & Sereno, M. I. Population receptive field tuning properties of visual cortex during childhood. *Dev. Cogn. Neurosci.* **37**, 100614 (2019).
10. Himmelberg, M. M. *et al.* Comparing retinotopic maps of children and adults reveals a late-stage change in how V1 samples the visual field. *Nat. Commun.* **14**, 1–15 (2023).
11. Arcaro, M. J. & Livingstone, M. S. A hierarchical, retinotopic proto-organization of the primate visual system at birth. eLife **6**, e26196 (2017).
12. Ellis, C. T. *et al.* Retinotopic organization of visual cortex in human infants. *Neuron* **109**, 2616–2626.e6 (2021).

13.Somerville, L.H. *et al.* The Lifespan Human Connectome Project in Development: A large-scale study of brain connectivity development in 5–21 year olds. *Neuroimage* **183**, 456–468 (2018).

14.Edwards, A. D. *et al.* The Developing Human Connectome Project neonatal data release. *Front. Neurosci.* **16**, 886772 (2022).

15.Haak, K.V. *et al.* Connective field modeling. *Neuroimage* **66**, 376–384 (2013).

16.Bock, A. S. *et al.* Resting-state retinotopic organization in the absence of retinal input and visual experience. *J. Neurosci.* **35**, 12366–12382 (2015).

17.Benson, N. C., Butt, O. H., Brainard, D. H. & Aguirre, G. K. Correction of distortion in flattened representations of the cortical surface allows prediction of V1-V3 functional organization from anatomy. *PLoS Comput. Biol.* **10**, e1003538 (2014).

18.Ment, L. R. *et al*. Preterm birth and the developing brain. *Lancet Neurol.* **7**, 378–379 (2008).

19.Zuberoa, M. Arriving too early. *Lancet Neurol.* **12**, 332–333 (2013).

20.Johnson, W. E., Li, C. & Rabinovic, A. Adjusting batch effects in microarray expression data using empirical Bayes methods. *Cereb. Cortex* **8**, 118–127 (2007).

21.Rakic, P. Prenatal genesis of connections subserving ocular dominance in the rhesus monkey. *Nature* **261**, 467–471 (1976).

22.Galli, L. & Maffei, L. Spontaneous impulse activity of rat retinal ganglion cells in prenatal life. *Science* **242**, 90–91 (1988).

23.Katz, L. C. & Shatz, C. J. Synaptic activity and the construction of cortical circuits. *Science* **274**, 1133–1138 (1996).

24.Huberman, A. D., Feller, M. B. & Chapman, B. Mechanisms underlying development of visual maps and receptive fields. *Annu. Rev. Neurosci.* **31**, 479–509 (2008).

25.Reid, V. M. *et al.* The human fetus preferentially engages with face-like visual stimuli. *Curr. Biol.* **27**, 1825–1828.e3 (2017).

26.Donovan, T., Dunn, K., Penman, A., Young, R. J. & Reid, V. M. Fetal eye movements in response to a visual stimulus. *Brain Behav.* **10**, e01676 (2020).

27.Del Giudice, M. Alone in the dark? Modeling the conditions for visual experience in human fetuses. *Dev. Psychobiol.* **53**, 214–219 (2011).

28.Ko, H., Cossell, L., Baragli, C., Antolik, J., Clopath, C., Hofer, S. B., & Mrsic-Flogel, T. D. The emergence of functional microcircuits in visual cortex. *Nature* **496**, 96–100 (2013).

29.McIntosh, A. R., Kovacevic, N. & Itier, R. J. Increased brain signal variability accompanies lower behavioral variability in development. *PLoS Comput. Biol.* **4**, e1000106 (2008).

30.Nomi, J. S., Bolt, T. S., Chiemeka Ezie, C. E., Uddin, L. Q. & Heller, A. S. Moment-to-moment BOLD signal variability reflects regional changes in neural flexibility across the lifespan. *J. Neurosci.* **37**, 5539–5548 (2017).

31.Williams, L. Z. J. *et al.* Structural and functional asymmetry of the neonatal cerebral cortex. *Nat. Hum. Behav.* **7**, 942–955 (2023).

32.Carney, O. *et al.* Incidental findings on brain MR imaging of asymptomatic term neonates in the Developing Human Connectome Project. *eClinicalMedicine* **38**, 100984 (2021).

33.Hughes, E. J. *et al.* A dedicated neonatal brain imaging system. *Magn. Reson. Med.* **78**, 794–804 (2017).

34.Fitzgibbon, S. P. *et al.* The developing Human Connectome Project (dHCP) automated resting-state functional processing framework for newborn infants. *Neuroimage* **223**, 117303 (2020).

35.Harms, M. P. *et al.* Extending the Human Connectome Project across ages: Imaging protocols for the Lifespan Development and Aging projects. *Neuroimage* **183**, 972–984 (2018).

36.Makropoulos, A. *et al.* The developing human connectome project: A minimal processing pipeline for neonatal cortical surface reconstruction. *Neuroimage* **173**, 88–112 (2018).

37.Cordero-Grande, L., Hughes, E. J., Hutter, J., Price, A. N. & Hajnal, J. V. Three-dimensional motion corrected sensitivity encoding reconstruction for multi-shot multi-slice MRI: Application to neonatal brain imaging. *Magn. Reson. Med.* **79**, 1365–1376 (2018).

38.Kuklisova-Murgasova, M., Quaghebeur, G., Rutherford, M. A., Hajnal, J. V. & Schnabel, J. A. Reconstruction of fetal brain MRI with intensity matching and complete outlier removal. *Med. Image Anal.* **16**, 1550–1564 (2012).

39.Tustison, N. J. *et al.* N4ITK: improved N3 bias correction. *IEEE Trans. Med. Imaging* **29**, 1310–1320 (2010).

40.Smith, S. M. Fast robust automated brain extraction. *Hum. Brain Mapp.* **17**, 143–155 (2002).

41.Makropoulos, A. *et al.* Automatic whole brain MRI segmentation of the developing neonatal brain. *IEEE Trans. Med. Imaging* **33**, 1818–1831 (2014).

42.Andersson, J. L. R., Skare, S. & Ashburner, J. How to correct susceptibility distortions in spin-echo echo-planar images: application to diffusion tensor imaging. *Neuroimage* **20**, 870–888 (2003).

43.Andersson, J. L. R. *et al.* Towards a comprehensive framework for movement and distortion correction of diffusion MR images: Within volume movement. *Neuroimage* **152**, 450–466 (2017).

44.Salimi-Khorshidi, G. *et al.* Automatic denoising of functional MRI data: combining independent component analysis and hierarchical fusion of classifiers. *Neuroimage* **90**, 449–468 (2014).

45.Glasser, M. F. *et al.* The minimal preprocessing pipelines for the Human Connectome Project. *Neuroimage* **80**, 105–124 (2013).

46.Jenkinson, M., Bannister, P., Brady, M. & Smith, S. Improved optimization for the robust and accurate linear registration and motion correction of brain images. *Neuroimage* **17**, 825–841 (2002).

47.Glasser, M. F. *et al.* A multi-modal parcellation of human cerebral cortex. *Nature* **536**, 171–178 (2016).

48.Wang, L., Mruczek, R. E. B., Arcaro, M. J. & Kastner, S. Probabilistic maps of visual topography in human cortex. *Cereb. Cortex* **25**, 3911–3931 (2015).

49.Fortin, J. P. et al. Harmonization of cortical thickness measurements across scanners and sites. *Neuroimage* **167**, 104–120 (2017).

Data availability

The data for this study are available after institutional registration through public links in the National Institute of Mental Health Data Archive (NDA). Prenatal and neonatal data are available at https://nda.nih.gov/edit_collection.html?id=3955. Adolescent and adult data are available at https://nda.nih.gov/edit_collection.html?id=2846.

Code availability

All data analysis was performed with custom software using Python 3.11 and various third-party packages (matplotlib 3.8.3, numpy 1.26.3, pandas 2.2.0, scipy 1.12.0, and nibabel 5.2.0). Brain surfaces were visualized with nilearn (0.10.4). All code used for data analysis is available from GitHub (https://github.com/SkeideLab/SPOT).

Acknowledgements

This work was supported by the German Research Foundation (DFG Heisenberg Program Grant 433758790 awarded to M.A.S.), the Alexander von Humboldt Foundation (M.A.S. was appointed to the Henriette Herz Scouting Programme) and the Jacobs Foundation (Research Fellowship awarded to M.A.S.). Data were provided by the developing Human Connectome Project, KCL-Imperial-Oxford Consortium funded by the European Research Council under the European Union Seventh Framework Programme (FP/2007-2013) / ERC Grant Agreement no. [319456]. We are grateful to the families who generously supported this study.

Author contributions

M.A.S. conceived the study. S.Y. and A.K. analyzed the data. S.Y. visualized the results with feedback from A.K. and M.A.S. S.Y. and M.A.S. wrote the manuscript. M.A.S. supervised the study.

Ethics declarations

The authors declare no competing interests.